Global tool path optimization of high-resolution image reproduction in ultrasonic modulation cutting for structural coloration

Yang Yang[a], Ping Guo[a,b,*]

[a] Department of Mechanical and Automation Engineering, Chinese University of Hong Kong, Hong Kong, China
[b] Department of Mechanical Engineering, Northwestern University, Evanston, IL, USA

A B S T R A C T

Diffraction gratings are capable of splitting and diffracting parallel white light into a wide diffractive spectrum containing light with different wavelengths travelling in different directions. The apparent angle-dependent color effect is a form of structural coloration. In this paper, a rendering strategy for grating-induced high-resolution image reproduction has been demonstrated based on tool path optimization. The grating structures are generated by ultrasonic modulation cutting due to the cutting depth modulation. The high-resolution image rendering is accomplished by tailoring the interaction between visible light and grating structures through the design and optimization of the distribution of machined grating arrays. Fabricating the desired grating arrays requires a complex objective tool path with ever-changing discontinuous step velocity profiles, which is not achievable for any existing machine tools considering the limited acceleration capability. Unlike conventional toolpath optimization methods, the proposed research aims to relate the cutting process to high-resolution image rendering performance and optimize the quality of machined images through optimally approximating the objective tool velocity-location curve with a series of parametric splines in terms of minimum overall velocity error. A recursive optimization method has been developed to ensure the global optimum of the tool velocity profile considering the physical limitation of motion axes. The fitting performance of proposed method is quantitatively analyzed and evaluated through the simulation and experiment by comparing the real-time velocity-location profiles to the objective curves. In addition, the reproduction quality of machined images is evaluated by measuring the similarity between the reproduced and original images with both simulation and experimental results.

1. Introduction

Apart from the pigment-based coloration, surface micro-structures serve as a primary contributor to the object color by physically manipulating the propagation of visible light at the interface. In fact, many kinds of striking structural color have been frequently found in nature including the wings of *Morpho* butterfly [1], iridescent feathers of peacock [2] and allochromatic elytra of *Hercules* beetle [3]. The structural color effect originates from the presence of micro/nano-scale delicate structures on the living creature surface and their complex optical interactions with visible light including diffraction, interference and scattering. Inspired by the structural coloration in nature, substantial researches have been dedicated to applying the structural coloration technology in an array of newly arising functional applications such as color printing, anti-counterfeiting and functional decoration [4,5].

Recent advances in nanofabrication techniques have paved the way to control the light propagation characteristics at the scale comparable to the wavelength of visible light. Guo and Vorobyev [6] were among the first to control the optical properties of metals with femtosecond laser induced periodic surface structures (LIPSSs). The orientation dependence of LIPSSs on the direction of laser polarization offers the possibility to render complex color image reproduction by tuning the polarization of femtosecond laser pulses [7]. However, the optimal operating parameters, such as laser fluence, to form orderly structures greatly rely on the surface plasmon resonance and hence need careful calibration for each material [6]. In addition, plasmonic nanostructures fabricated by e-beam lithography or focused ion beam lithography have been reported to possess unique angle-independent color effect [4,5,8]. As demonstrated in Ref. [8], micro-image printing based on plasmonic color shows great potential as the next-generation printing technology due to the advantages of sub-diffraction-limit printing resolution and

Nomenclature

λ	wavelength of diffracted light (µm)
P_{max}	maximal pixel number in one segment
s	line spacing of gratings (µm)
P_{min}	minimal pixel number in one segment
θ_i	incident angle of parallel white light (°)
$\hat{v}$	velocity resolution of the motion axis
θ_k	observing angle (°)
d	pixel length in the cutting direction
K	diffracted order
Acc^*	axis maximal allowable acceleration
δ	grating angular dispersion
T	running time for each cubic spine profile
$m(t)$	tool cutting motion profile
v_{max}	maximal velocity in the processed segment
f	vibration frequency of cutting tool (kHz)
v_{min}	minimal velocity in the processed segment
X	cutting direction
E^*	optimal fitting error for a series of pixels
Y	cross-feed direction
$v(i)$	objective tool velocity at the ith pixel in the processed segment
i	region index for each row
$V_{fit}(X)$	optimized tool velocity at the position X in the processed segment
$F(i)$	overall fitting error for the ith region
$acc_{critical}$	critical acceleration gap
$L_i(k)$	pixel number in the kth segment of ith region
r	pixel number employed in the processed fitting step
R_i	pixel number in the ith region
M_i	segment number in the ith region
k	segment index for each region
Λ	feasible region of pixel number in each segment

full color capability without any pigment material. Nevertheless, plasmonic color operating at the resonance mode has strict requirement on the fabrication accuracy of nanostructures and the narrow bandwidth of working frequency. In our previous study, a mechanical machining method utilizing ultrasonic modulation has been demonstrated to be able to generate submicron-scale grating structures with high speed and low cost on various metallic surfaces such as aluminum alloy, stainless steel, brass, copper, etc. [9]. The proposed modulation machining method is an extended technology inspired by ultrasonic vibration-assisted cutting, which utilizes a micro-amplitude and high-frequency depth-of-cut modulation to efficiently generate periodic micro/nanoscale structures with controllable spatial interval and orientation [10–12]. Controllable micro/nano-structures have been utilized to generate delicate patterns and images for functional applications. Suzuki et al. [13] have demonstrated ultra-precision sculpturing of novel patterns utilizing an amplitude-controlled vibration-assisted machining method. The tool path planning is established by synchronizing the tool vibration amplitude with the tool feeding position to obtain desired cutting depths at each pixel of reproduced patterns. Similar work has been conducted in ultra-precision diamond turning process by engraving inverted pyramid structures with different geometry as the constituent pixels of a grayscale image [14]. The optimal tool path is constructed by fitting the image data points with a family of Archimedean spiral paths in terms of minimum machining error. Although the feasibility to generate complex patterns and grayscale images with surface micro/nanostructures has been demonstrated, few research attempts have been made to render high-resolution color images based on structural coloration using a mechanical machining method.

Although the structural coloration based on diffraction effect has been demonstrated in our previous paper using ultrasonic modulation cutting process [9], the process capability extension for high-resolution image rendering requires a deeper understanding of image formation mechanism and its relationship to the proposed cutting process. The process parameters, especially the nominal cutting velocity, play key role in determining the modulation-induced grating formation mechanism and the induced diffraction effect. Programming and optimizing the tool velocity profile are of great importance for the generation of image inducible grating structures. The construction of simulation model for predicting the image rendering performance is highly desired as well.

In this paper, an effective implementation algorithm has been proposed to reproduce high-resolution images with the vibration-induced grating structures based on tool path planning. Unlike the conventional tool path planning methods [14–17], where the objective is to minimize the machining error and duration by approximating a surface with a family of segments and arcs, the proposed research aims to relate the cutting process to high-resolution image rendering performance and optimize the quality of machined images through optimally approximating the objective tool velocity-location curve with a series of parametric splines in terms of minimum overall velocity error. Based on the rendering principle of grating-induced structural coloration, the goal of realizing high-resolution image reproduction is equivalent to generate a desired tool path whose velocity-location profile is a piecewise step function. Considering the limited acceleration capability of motion axes and ultra-small pixel size ($\sim 10^{-2}$ mm) of the high-resolution image, it is impossible to generate the desired constant cutting velocity within each pixel due to the unavoidable transition distance for changing the velocity of cutting axis. Many researchers have been dedicated to the designs of various interpolators for non-uniform rational B-spline (NURBS) to approximate the parametric curves with compact programming code size [18–20]. However, such tool path planning strategies are not suitable for this case since the ideal velocity profile is a discontinuous function. In addition, NURBS has not been widely supported by many commercial CNC controllers. Thus, a parametric optimization procedure is firstly established by fitting a given series of data points in the objective velocity-location curve with a cubic polynomial spline in terms of minimum velocity error. The feasible region of segment length, or pixel number, is constrained by the minimum sampling time and acceleration capability of the motion axis. A recursive searching method then is developed to optimally divide the objective tool velocity-location profile into a series of segments in terms of global minimum velocity error. The performance of proposed tool-path planning method is evaluated through quantitatively analyzing the overall fitting accuracy and simulation of reproduced color images based on the optimal tool paths. The feasibility and effectiveness of the global tool path optimization algorithms are experimentally investigated by comparing the real-time tool velocity-location profiles to the objective curves and evaluating the quality of reproduced color images through measuring the similarity between the machined and original color images with an image comparison method. In addition to the high-resolution image reproduction, the outcome of this paper might provide insights to other tool path optimization problems that require additional control over tool velocity, such as three-axis CNC machining [21] and high-speed machining [22].

The remaining part of this paper is arranged as follows. Section 2 illustrates the process principle of grating-induced high-resolution image reproduction. Section 3 discusses the implementation of tool path planning algorithm. Section 4 analyzes the effectiveness of proposed implementation algorithm through image simulation. Section 5 provides the experimental verification with ultrasonic modulation cutting of high-resolution color images and the evaluation of image reproduction quality. Conclusions are given in Section 6.

2. Methodology

2.1. Grating arrays machined with ultrasonic modulation cutting

To make the description of overall image reproduction process complete, previous work related to the principle of grating structure generation is introduced in this sub-section. The further details can be referred to the authors' previous work [9]. Elliptical vibration texturing has been demonstrated to be a promising manufacturing process for the generation of surface structures in the micro- and nano-scale range due to their impressive features such as high efficiency, accuracy and scalability for industrial production [23–25]. As illustrated in Fig. 1, when the elliptically vibrated cutting tool is fed along the machined surface with a relatively low cutting velocity, periodic grating-like structures perpendicular to the cutting direction will be left on the finished surface. The cutting operation is sequentially carried out in parallel lines, where the grating width is determined by the tool geometry and the cross feed. In addition, the grating line spacing (s) is related to the cutting motion, m(t), and given by:

$$s = \frac{1}{f} * \frac{dm(t)}{dt} = \frac{v(t)}{f} \tag{1}$$

The main difficulty to generate the sub-micron grating structures lies in the development of ultrafast tool actuation to ensure a stable cutting process and improve the process efficiency. In addition, the grating line spacing accuracy is related to the tool vibration frequency and velocity accuracy of employed motion axis. A higher tool vibration frequency is in favor to increase the line spacing accuracy of obtain gratings since it is challenging to achieve high velocity control over small velocity region. Our cutting tool works at the resonant mode with a designed resonant frequency in the ultrasonic range (~ 30 KHz), which enables the concurrent generation of nearly 30 thousand periodic groove structures per second. The ultrasonic tool vibration also allows the generation of submicron-scale grating with an acceptable nominal cutting velocity (~ 30 mm/s) in terms of machining efficiency. Moreover, the grating spacing is tunable by programing the nominal velocity of cutting motion based on Eq. (1). Ideally, the vibration-induced structures, machined with a piecewise step velocity profile, have a corresponding piecewise step grating spacing profile as shown in Fig. 1. Periodic grating structures with different spacing distances lie in the sub-micron range could serve as reflection type diffraction elements

and introduce distinct iridescent color.

2.2. Rendering principle of high-resolution image reproduction

Structural color arising from diffraction can be utilized as color palettes to render high-resolution images by applying the insight gained from the basic grating equation. When the parallel white illumination condition is employed, the wavelength (λ), or say color, of diffracted light travelling in the observed direction is governed by Ref. [26]:

$$\lambda_{\theta_k} = \frac{s(\sin \theta_k + \sin \theta_i)}{K} \tag{2}$$

Since the light intensity tends to decrease tremendously for higher order diffraction leading to the brightness reduction of diffracted color, the diffracted order (K) is assumed to be 1 in this study. If the observing direction is perpendicular ($\theta_k = 0$) to the grating surface, the diffracted color is then determined by the incident angle (θ_i) and line spacing of the grating structures.

Considering that the generation of while light with absolute parallelism is very challenging, the angular dispersion (δ) of gratings is defined as follows:

$$\delta(\lambda) = \frac{d\theta_i}{d\lambda} = \frac{\tan \theta_i}{\lambda} \tag{3}$$

It describes the tolerance angle of incident parallel white light to render the desired structural color with a specific wavelength, as shown in Fig. 1. Therefore, a larger incident angle is favorable for obtaining larger angular dispersion. On the other hand, a larger incident angle will result in limited energy remaining for diffraction reflection due to the higher energy loss in spectral reflection [27]. In this study, the incident angle of parallel white light is fixed at 45° to keep a balance between the angular dispersion and energy loss in spectral reflection. With the above assumptions, structural color represented by a specific dominant light wavelength can be implemented using diffractive gratings with corresponding line spacing based on the following equation:

$$s = \frac{K*\lambda}{\sin \theta_k + \sin \theta_i} = \frac{\lambda}{\sin(45°)} \tag{4}$$

As illustrated in Fig. 1, under the identical incident and observing angles, grating structures with a larger line spacing will diffract light with a larger wavelength, while grating structures with a smaller line
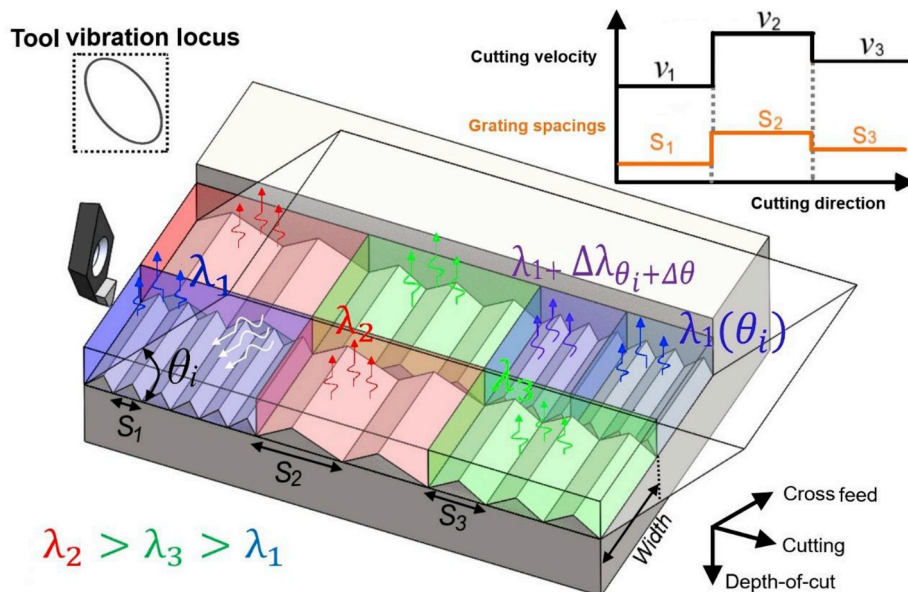

Fig. 1. Schematic of grating structures containing variable spacing distances induced by ultrasonic modulation cutting and the corresponding diffractive structural color effect. (For interpretation of the references to color in this figure legend, the reader is referred to the Web version of this article.)

spacing will introduce structural color with a smaller wavelength. Therefore, the goal of realizing pixelated color image reproduction with prescribed color at each pixel is equivalent to generate grating structures with corresponding line spacing at each pixel of the reproduced color image. Since the rendering range of diffracted structural color is directly mapped from the whole visible spectrum, achromatic color that cannot be represented by any visible light is, therefore, out of the proposed color palettes.

Considering that the color information of digital images is usually mathematically described and stored by a three-dimensional color space, such as RGB and HSV, it is necessary to establish a mapping function from the diffracted structural color, differentiated by the wavelength of light, to the color displaced on a computer monitor. One of the main advantages of HSV over RGB color space is that the main color attribute can be represented by only the hue axis instead of the three axes in RGB color space [28]. Therefore, the perceptual hue is usually regarded as a digital analog of the dominant wavelength of spectrum color. Constrained by the spectral response sensitivity of CMOS imaging sensors, the wavelength range of visible spectrum is determined to be from 0.41 μm to 0.71 μm. In addition, since the hue axis is a circle where the color sequence is arranged as the same of visible spectrum but with the purple segment connected to red segment, we adopt the following calibrated linear transfer functions to link the hue to the wavelength:

$$\text{wavelength } (\lambda) = \begin{cases} -0.26 * Hue + 0.64, & Hue \in [0,\ 0.9) \\ 0.70 * Hue + 0.01, & Hue \in [0.9,\ 1] \end{cases} \quad (5)$$

The calibration process can be established by extracting the hue of captured diffractive color and mapping it to the wavelength given by Eq. (2) under different illuminating and observing conditions. The detailed descriptions about the calibration process and derivation of function coefficients are discussed in Appendix 3. It is noted that the adopted linear relationship between the color hue and light wavelength is an approximation based on the color matching. As the hue is essentially one-dimension representation in HSV color space and the exact color of diffracted light depends on the light intensity as well, it is impossible to establish the precise relationship between the color hue and light wavelength.

The overall flowchart for reproducing the high-resolution image with diffractive structural color is shown in Fig. 2. Firstly, the digital color images are pre-processed using $MATLAB^{\circledR}$ software, where the hue of each pixel is extracted and used as an indicator to distinguish different color. Secondly, the hue value is linearly mapped to the

wavelength from 0.41 μm too 0.71 μm based on Eq. (5). After that the derived wavelength matrix is transformed to an objective velocity matrix based on Eq. (1) and Eq. (4). It is noteworthy that the pixel size in the cutting (X) and cross-feed (Y) directions could be anisotropic. It has a higher resolution in the cutting direction, which is constrained by the motion axis capabilities, while the cross-feed resolution is a function of the tool geometry and adopted cross feed. The objective velocity matrix should be compressed accordingly in order to ensure un-stretched image reproduction. Thirdly, the global optimization procedure is carried out based on the objective velocity matrix and other selected machining parameters. Fourthly, the fitting performance is evaluated through the quantitative analysis of fitting accuracy and the simulation of reproduced color images based on the optimized tool path. Fifthly, the machining process is executed with the aid of ultrasonic elliptical vibration after downloading the optimal tool motion program to the motion controller. The real-time velocity-location profiles are collected and compared to the commanded tool paths to validate the feasibility of optimized tool path. Finally, the rendering quality of reproduced color images are evaluated to demonstrate the effectiveness of the proposed tool path planning algorithm.

3. Tool path planning algorithm

In order to optimize the quality of reproduced color images, the goal of tool path planning is to achieve the global minimal velocity error between the actual tool path and the objective one specified by the ideal velocity matrix. The ideal tool cutting velocity profile is a discrete function where a constant velocity is specified inside each pixel of the color image. An intuitive idea to program the tool path is to command constant velocity inside each pixel. This can be implemented utilizing the linear interpolation command in G-code (G01) of the CNC machine, where the servomotor is commanded to move the cutting tool from a start point to an end point with a specified velocity. However, this simple idea is not able to achieve the desired objective motion profile due to the small pixel size ($\sim 10^{-2}$ mm) and the limited acceleration capability of motion axis. Moreover, the velocity profile in the acceleration region may vary greatly among different CNC machines equipped with various types of servomotors. The velocity overshooting caused by inappropriate setting of acceleration curve and rate will significantly deteriorate the machining accuracy and quality of generated grating structures or even lead to cutting instability. Although pixel downscaling can be used for practical implementation by re-assigning an identical velocity to several nearby pixels with their averaged values, it is at the expense of partially losing the detailed
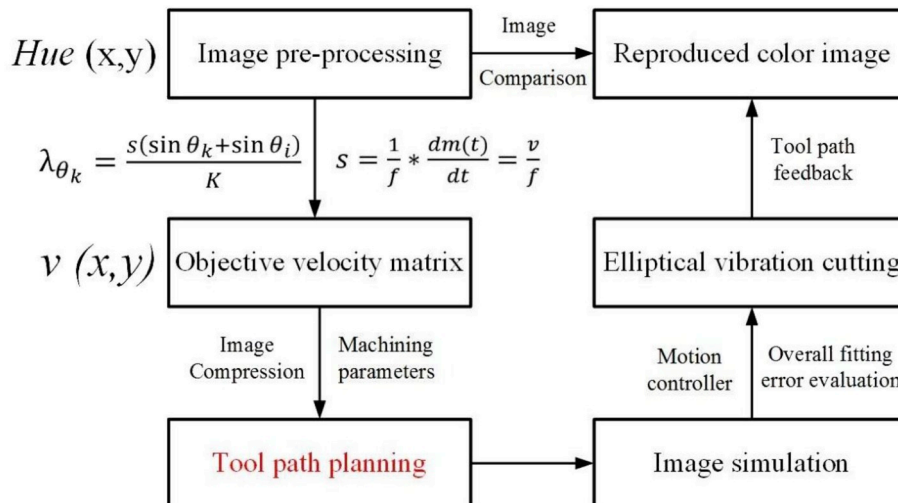

Fig. 2. Overall flowchart for reproducing the color image with diffractive structural color. (For interpretation of the references to color in this figure legend, the reader is referred to the Web version of this article.)

information of original high-resolution image.

3.1. Tool path planning using cubic spline interpolation command (PVT)

In this paper, we propose a method to plan the tool path by optimally fitting the objective tool path with a series of continuous spline functions considering the physical limitation of motion axis. Two key optimization procedures will be involved in the global tool path optimization process. The first one is to minimize the velocity error and to calculate corresponding spline parameters for a given series of data points in the objective velocity matrix. Based on the minimized optimal fitting error, the second one is to identify the globally optimized division of each cutting line into a series of segments in terms of minimum overall velocity error. The overall optimized tool path then can be constructed by sequentially connecting the optimal spline functions in each divided segment.

In this paper, the spline used to approximate a given series of data points is a cubic polynomial function as given by

$$x(t) = x_{t_i} + c_i(t - t_i) + b_i(t - t_i)^2 + a_i(t - t_i)^3 \qquad (6)$$

One approach to numerically determine the three unknown coefficients is to specify the final position (x_{t_i+T}), running time (T_i) as well as the start velocity (v_{t_i}) and end velocity (v_{t_i+T}) of the running segment. Then the unknown coefficients can be solved by the following equations:

$$a_i = -\frac{2(x_{t_i+T_i} - x_{t_i})}{T_i^3} + \frac{v_{t_i+T_i} + v_{t_i}}{T_i^2} \qquad (7)$$

$$b_i = \frac{3(x_{t_i+T_i} - x_{t_i})}{T_i^2} - \frac{v_{t_i+T_i} + 2v_{t_i}}{T_i}$$

$$c_i = v_{t_i}$$

The motion controller will use the above cubic polynomial function

to interpolate between the start and end points of the segment. For consecutive cubic motion profiles, only the final position (P), end point velocity (V) and running time (T) should be specified in order to ensure the continuity of position and velocity at each segment extremity, which is therefore called PVT (Position-Velocity-Time) command. It should be emphasized that the running time for each cubic polynomial movement can only be integer in millisecond for the practical implementation in commercially available CNC controllers considering the minimum sampling period, the effect of which on the fitting performance will be discussed further in detail.

Apart from the higher fitting accuracy than linear or quadratic polynomial motion profiles for tool path approximation, the attractiveness of PVT command is that the function coefficients do not depend on the information of previous segments but only depend on the information of processed segment, which is computationally friendly compared to other higher order interpolation methods. In addition, each PVT command will impose continuously changing smooth velocity profile, which is favorable for gradient color information reproduction. Even though the continuity condition of acceleration between each segment is not satisfied with the above interpolation method, it is beneficial for highlighting the edge feature due to jerk motion and providing a wider fitting range for tool path planning. However, the change of acceleration at the connection points of two nearby segments should be set within a critical value to prevent possible machining instability:

$$\Delta_{acc} = acc_{t_{i+1}} - acc_{t_i+T_i} < acc_{critical} \qquad (8)$$

3.2. Determination of the overall objective function

The flow diagram of global tool path optimization algorithm for one cutting line is shown in Fig. 3. If the optimal fitting velocity error for a given series of data points in the objective velocity matrix can be provided, the global optimal division method to divide each cutting line
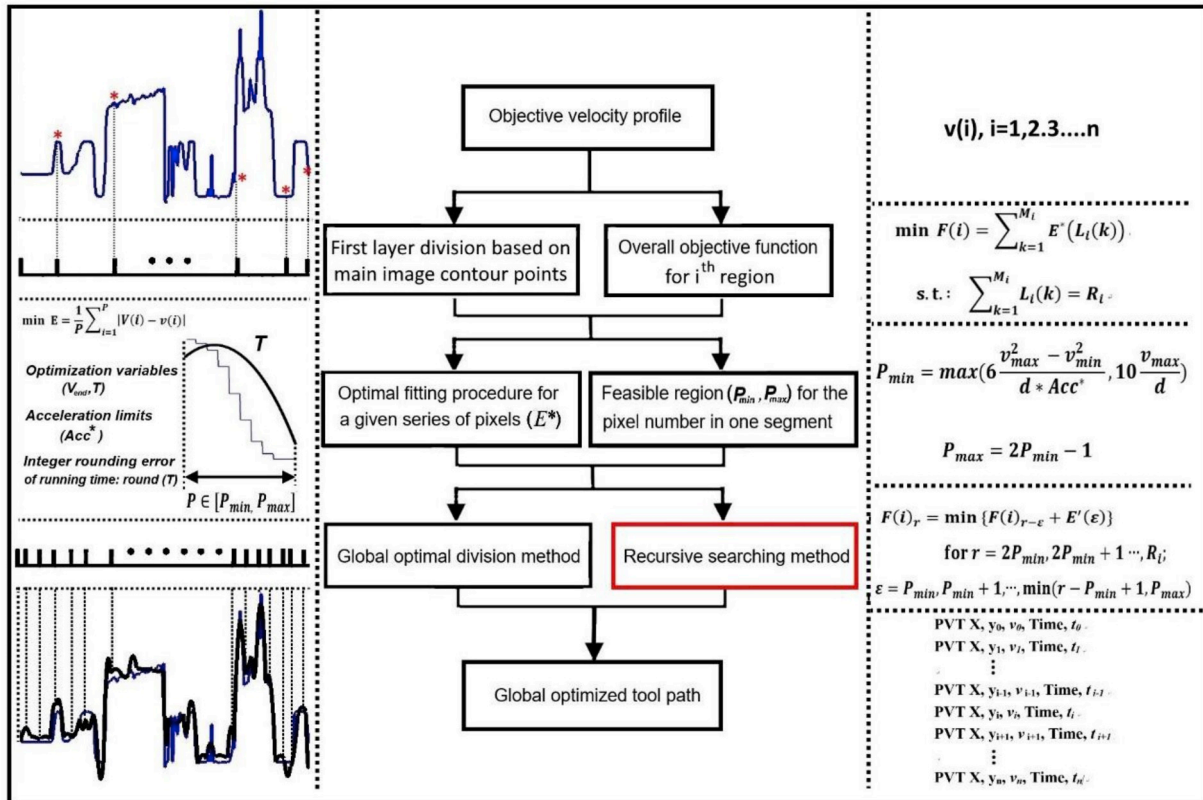

Fig. 3. Flow chart of the global tool path optimization for one cutting line in the objective tool velocity matrix.

into a series of segments can be identified by searching the minimum sum of velocity error of all segments among all the possible division candidates. Since the computation complexity increases rapidly with the total pixel number in each cutting line, the main image contour points can serve as candidate control points to firstly divide each cutting line of the objective velocity matrix into several regions. The term, region, can be regarded as the first layer division for each cutting line. Then the global optimal division algorithm is sequentially applied within each region for the final division. The optimization algorithm keeps searching for a series of control points to optimally divide each region into several segments and fit each segment with one optimal cubic polynomial function. Therefore, the optimization procedure can be carried out region by region. The overall objective function ($F(i)$) and constraints for the ith region of each cutting line are defined as follow:

$$\min F(i) = \sum_{k=1}^{M_i} E^*(L_i(k)) \tag{9}$$

$$\text{s.t. :} \quad \sum_{k=1}^{M_i} L_i(k) = R_i \tag{10}$$

$$L_i(k) \in \Lambda, \quad k = 1, 2, \dots M_i \tag{11}$$

where R_i is the pixel number in the ith region of each cutting line; $L_i(k)$ is the pixel number in the kth segment. Λ is the feasible region of pixel number in each segment for one polynomial function fitting and $E_i^*(k)$ is the optimal fitting error in the kth segment, both of which will be discussed in detail in section 3.3.

3.3. Optimization procedure for a given series of pixels with pixel number of $L_i(k)$ and determination of the feasible region of $L_i(k)$

This subroutine needs to provide the optimal fitting error as well as the corresponding fitting parameters for a given series of pixels. The employed fitting function is a cubic polynomial with respect to time. In order to ensure the continuity of velocity and position, the end position and start point velocity should be prescribed. Then, there will be two optimization variables, namely the end point velocity ($V(L_i(k))$) and running time (T) of the segment. The feasible region for the two optimization variables are set as follows:

$$V(L_i(k)) \in [v(L_i(k)) - \hat{v}, v(L_i(k)) + \hat{v}] \tag{12}$$

$$T = integer; \text{ and } T \in \left[round\left(\frac{L_i(k)d}{v_{max}}\right), round\left(\frac{L_i(k)d}{v_{min}}\right) \right]$$

where $v(i)$ is the objective velocity at the ith pixel of the segment; $\hat{v}$ is

the minimal velocity increment constrained by the employed encoder resolution of the motion controller. Then the objective function is to minimize the average of differences between the fitted velocity and objective velocity at each pixel:

$$E^*(L_i(k)) = \min \ E(L_i(k)) = \frac{1}{L_i(k)} \sum_{i=1}^{L_i(k)} |V(i) - v(i)| \tag{13}$$

The function $V(X)$ is the fitted velocity profile with respect to the position instead of time, which can be obtained by firstly calculating the coefficients of fitted cubic polynomial using Eq. (6) and Eq. (7), and then evaluating the fitted velocity at each pixel position by solving the corresponding time to reach each pixel in the fitted cubic polynomial.

It should be noted that the optimal fitting performance greatly relies on the objective velocity profile of given pixels as well as the overall pixel number. On the one hand, fewer pixels for one cubic polynomial fitting is favorable to achieve a lower average fitting error. On the other hand, significant integer rounding error of the running time will be introduced for the segment containing limited pixels. Typical fitting performance for a given series of pixels in the objective velocity matrix is shown in Fig. 4. It can be seen that although the optimal fitting error can reach $1.00 \, \text{mm s}^{-1}$/pixel with a corresponding running time of 4.5 ms for the segment containing 6 pixels, the integer rounding operation will greatly deteriorate the overall fitting performance. While the impact of integer attribute of the running time on the overall fitting performance can be negligible for the segment containing 40 pixels due to the much larger optimal running time. In addition, the maximal achievable acceleration rate (Acc_{max}) along the fitting spline is related to the overall pixel number in segment as well. Based on the feasible region of the optimization variables, the maximal acceleration rate can be bounded by the following equation:

$$Acc_{max} < 6 \frac{v_{max}^2 - v_{min}^2}{d * L_i(k)} \tag{14}$$

where v_{max} and v_{min} are the maximal and minimal velocities in the processed segment, respectively; d is the length of each pixel in the cutting direction. Therefore, the minimum pixel number in each segment should be constrained under the consideration of acceleration capability of motion axis and the integer attribute of the running time. If the minimal running time for each cubic polynomial movement is set larger than 10 ms to reduce the impact of integer rounding operation and the maximal allowable acceleration rate of the cutting axis is given by Acc^*, then the minimal pixel number in one segment is defined as follow:

$$P_{min} = max\left(6 \frac{v_{max}^2 - v_{min}^2}{d * Acc^*}, \ 10 \frac{v_{max}}{d} \right) \tag{15}$$
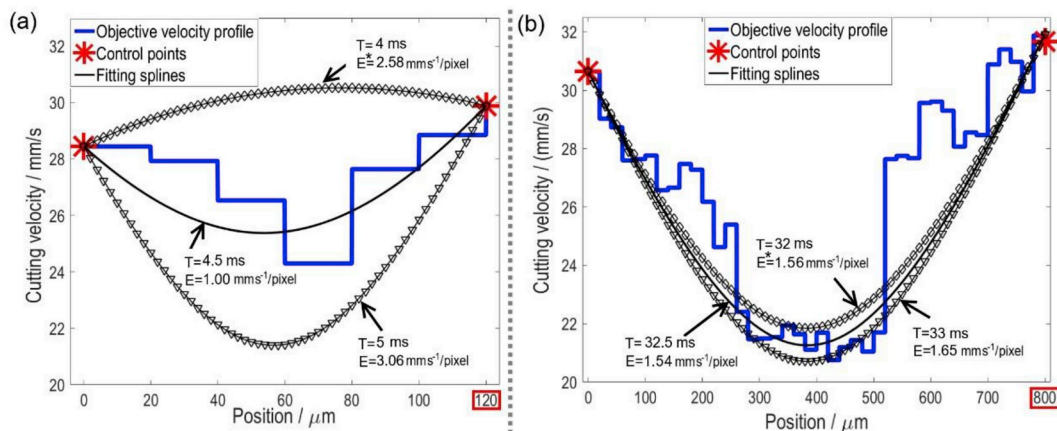

Fig. 4. Typical fitting operation for a given series of pixels containing different pixel number: (a) 6 pixels and (b) 40 pixels. The length of each pixel is 20 μm in the cutting direction.

Under the assumptions that the maximal acceleration rate (Acc^*) is 10,000 mm/s^2 (~ 1 g), and the length of pixel (d) is 20 μm in the cutting direction, the typical range of P_{min} in our study is from 10 pixels to 22 pixels. After the selection of minimal pixel number in one segment, the maximal allowable pixel number determines the upper bound of the feasible search region. Although a wider feasible pixel number range is theoretically favorable for the global optimization, the benefit of providing a wider feasible pixel number range will be gradually capped due to the increment of optimal fitting error resulted from the increase in pixel number for polynomial function fitting. Balanced by the overall fitting performance and the computation complexity of optimization process, the maximal pixel number in one segment is defined as follow:

$$P_{max} = 2P_{min} - 1 \tag{16}$$

3.4. Global optimization of the overall objective function

The remaining question is to determine the global optimal dividing method to divide each region into a series of segments in terms of the global minimal velocity error. Here, a recursive search method is proposed to ensure the global optimum of fitting accuracy. Firstly, when the pixel number in some region (R_i) is less than $2P_{min}$-1, the unique choice is to fit all the pixel in the region with one cubic polynomial. Otherwise, the initial values are calculated and stored using the first $2P_{min} - 1$ pixels in the region and given by:

$$F(i)_r = E^*(r), \qquad r = P_{min}, P_{min} + 1, \cdots 2P_{min} - 1, \qquad for\ R_i > 2P_{min} - 1 \tag{17}$$

Then an extra pixel in the subsequent position is added to first $2P_{min} - 1$ pixels for processing. By searching all the possible partition methods to divide the $2P_{min}$ pixels into several segments (M_i) and calculating the corresponding optimal fitting error in each segment, the optimal partition can be identified by finding the minimal sum of objective value in all segments. As a side note, the pixel number in each segment should lie in the feasible region of $L_i(k)$. After that, the optimal partition method for the first $2P_{min}$ pixels is recorded by saving the corresponding partition (control) points for the following iteration. The above process is repeated by adding one more extra point in the subsequent position until the last pixel in the region is considered. It is noteworthy that when the processed pixel number (r) is more than $P_{min} + P_{max}$-1, only the divided segments involving the last P_{max} pixels in the region are needed to be considered since the first r-P_{max} pixels have been calculated in the previous steps. The recursive equation is illustrated as follow:

$$F(i)_r = \min \{F(i)_{r-\varepsilon} + E'(\varepsilon)\}$$

for $r = 2P_{min}, 2P_{min} + 1 \cdots, R_i$;

$$\varepsilon = P_{min}, P_{min} + 1, \cdots, \min(r - P_{min} + 1, P_{max}) \tag{18}$$

where $E'(\varepsilon)$ is the optimal fitting error using the last ε pixels in the region and can be obtained using the algorithm discussed in section 3.3.

$$E'(\varepsilon) = E^*(r - \varepsilon + 1 \sim r) \tag{19}$$

The underlying essential of the above recursive searching method is to ensure the global optimum condition for all pixels in the region by recursively adding pixels to the previous optimal state.

For comparison, an intuitive method is to equally divide each cutting line into several segments in terms of segment length and fit each segment with one optimal cubic motion profile, which is computationally friendly but only feasible to get a local optimal tool path with respect to the adopted segment length. Besides, the approximation performance greatly depends on the given objective velocity profile and the determination of segment length. One example for fitting an array of pixels in the objective velocity matrix with different optimization methods is illustrated in Fig. 5.

4. Simulation of the reproduced color image and evaluation of the approximation performance

As discussed in section 3.4, an intuitive tool path planning method is to equally divide each region into several segments in terms of segment length and fit each segment with one cubic spine profile of optimal fitting parameters given by section 3.3. In order to predict the rendering performance of reproduced images machined with different optimized tool paths, the simulation of textured images is conducted with the aid of reverse process of rendering principle shown in Fig. 2. The color saturation and brightness at each pixel are assumed to be identical for the simulated results. Moreover, the approximation performance of different optimization methods is quantitively evaluated by two standard measures of difference between the objective velocity profile and optimized velocity profile, which are *RMSE* (root-mean-square error) and R^2 (coefficient of determination) defined as follow:

$$\text{RMSE} = \sqrt{\sum_{i=1}^{n} (V(i) - v)(i)^2/n} \tag{20}$$

$$R^2 = 1 - \sum_{i=1}^{n} \left(V(i) - v)(i)^2 / \sum_{i=1}^{n} (v(i) - \bar{v} \right)^2 \tag{21}$$
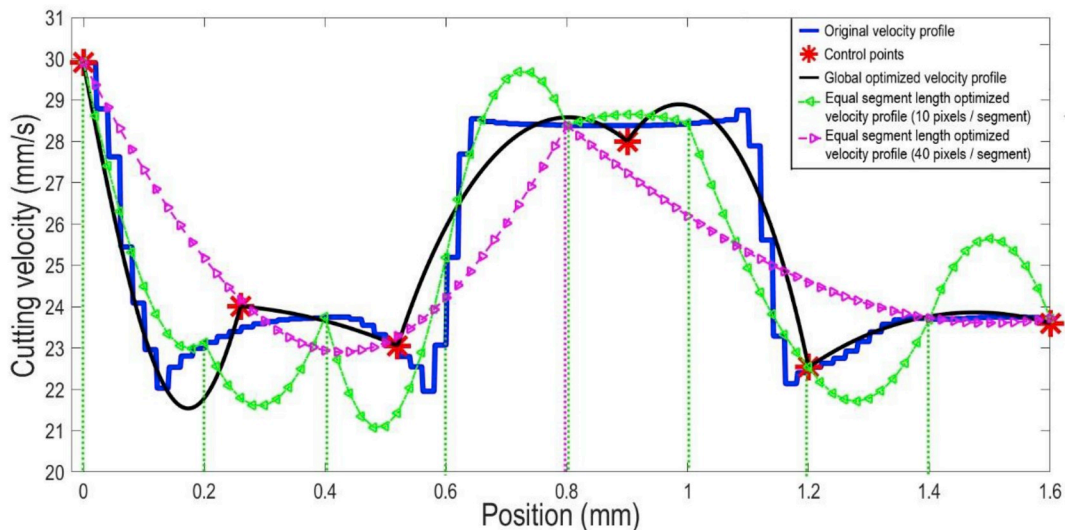

Fig. 5. Exemplary optimized tool velocity profile for approximating an array of pixels in the objective velocity matrix.

The RMSE can be regarded as an indicator of the average fitting error between the objective and optimized velocity at each pixel. In statistics, the R^2 is a measure of the proportion of variance of response variable that is predictable from the independent variables. It can be used as an estimator of overall fitting performance of different optimization methods, where a higher R^2 implies a better overall fitting accuracy.

The color image simulation results based on two different equal segment length optimization methods and the proposed global optimization method are shown in Fig. 6, while the fitting accuracy performance is presented in Table 1. It can be seen that the main contour of image is well described but appears to be artificially sharpened when the segment length equals to 10 pixels. Besides, the simulated image shows unexpected fringe patterns at the orange color regions. A fewer pixel number in each segment length leads to a higher overall fitting accuracy and brings a vivid reproduced color image with well-described image contour, while the resulting substantial control points are not favorable for depicting gradient color information and bring significant sharpening effect. The unexpected fringe patterns are mainly due to the uniform integer rounding error of the running time for each segment, which will be further revealed and discussed in section 5.3. On the other hand, the simulated image seems smoother and does not contain any unexpected fringe patterns when an equal segment length of 40 pixels is adopted. A longer segment length will decrease the number of control points in each cutting line and weaken the impact of integer rounding error on the fitting accuracy. However, the image becomes blurry and distorted as the fitting accuracy is greatly reduced compared to the equal segment length of 10 pixels. For the globally optimized tool velocity profile containing segments with varying pixel number, the simulated image inspiringly shows a clear image main contour together with smooth and vivid gradient color information that could not be achieved simultaneously by the above equal segment length optimization methods. The average and overall fitting accuracy is therefore better than the above equal segment length optimization methods, which supports the global optimality of the proposed optimization

Table 1
Fitting accuracy for different optimization methods.

	RMSE (mm/s)	R^2
Equal segment length of 10 pixels	1.06	0.83
Equal segment length of 40 pixels	1.43	0.69
Global optimization method	0.91	0.87

method. It is worth mentioning that the accuracy of predicted images still depends on the practicability of optimized tool paths.

5. Experimental verification

5.1. Experimental setup

The whole machining process was carried out on a custom-built CNC machining center. As configured in Fig. 7(a), the cutting motion was provided by a servomotor-driven linear actuator (*Aerotech ACT 165DL*) equipped with a non-contact linear encoder for online position monitoring. The position resolution of the linear actuator is 10 nm, while the velocity resolution is approximately 0.5 mm/s at a moving speed of 30 mm/s. A tertiary vibration generator [12] was mounted on the linear actuator to deliver the desired elliptical vibration to the cutting tool. In order to accurately generate grating structures with a feature size in the sub-micron range, a commercial single crystalline diamond tool with a nose radius of 200 μm, a rake angle of 0° and a clearance angle of 12° was employed for the cutting operation. Besides, the micro-scale depth-of-cut and cross-feed were set by a three-axis positioning stage (*Aerotech ANT130-060-L*), whose positioning resolution and repeatability are 1 nm and 75 nm. A tilting adjustment stage was employed to connect the three-axis stage and workpiece for ensuring the workpiece parallelism. The brass workpiece was pre-polished to achieve a mirror surface finish for the following experimental verification. The whole machine setup was controlled by an A3200 control
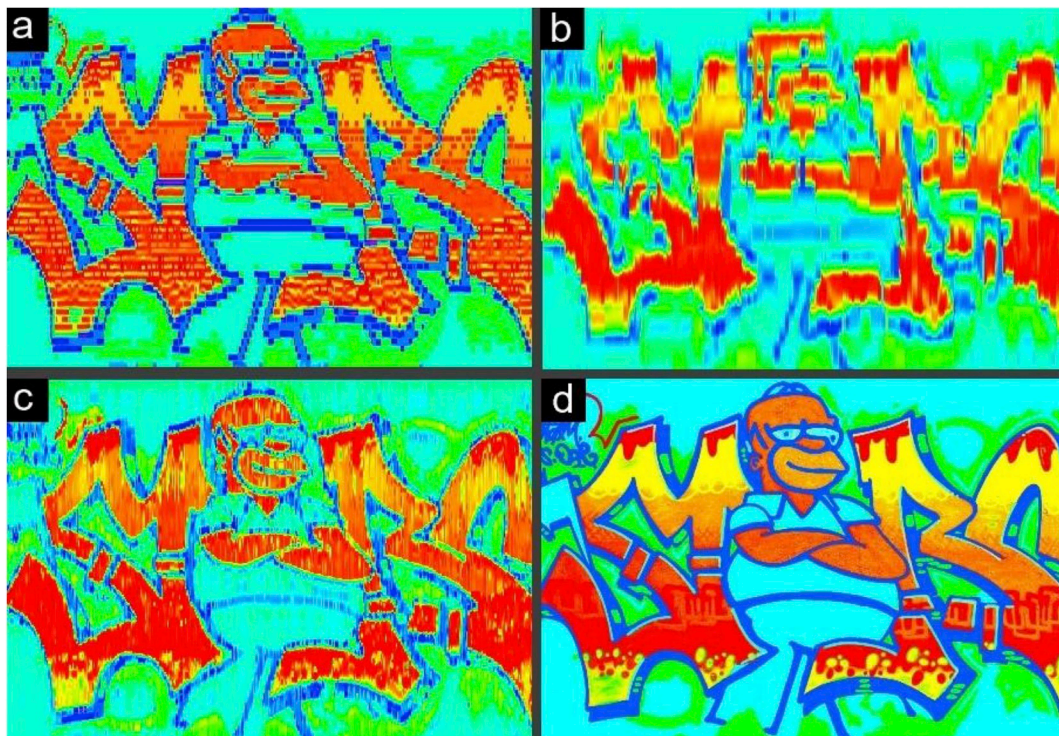
Fig. 6. Simulation of reproduced color images based on the optimized velocity matrix: (a) equal segment length of 10 pixels; (b) equal segment length of 40 pixels; (c) global optimization method containing segments with varying pixel number; (d) original image (350 × 485 pixels). The length of each pixel is 20 μm in the cutting direction. (For interpretation of the references to color in this figure legend, the reader is referred to the Web version of this article.)
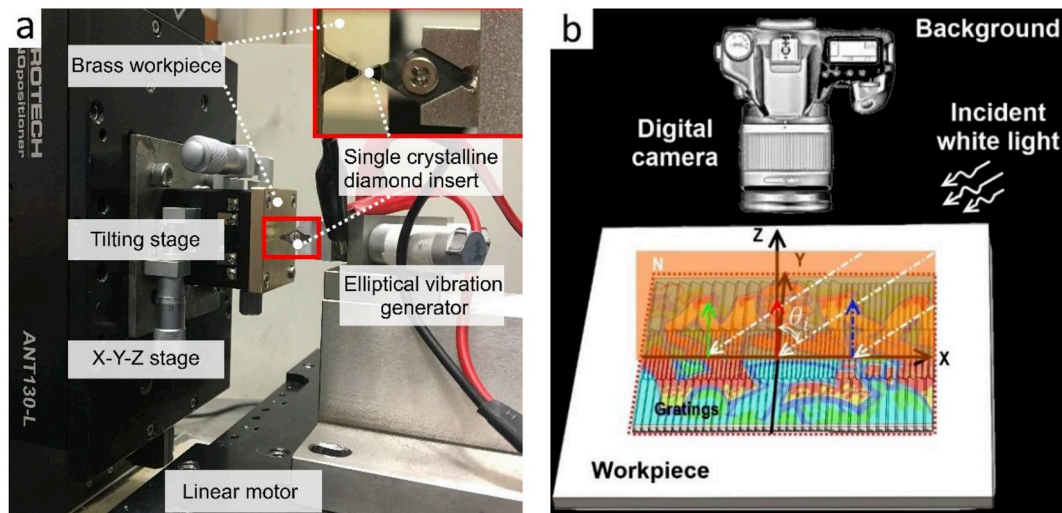
Fig. 7. (a) Experimental setup of the ultrasonic modulation cutting; and (b) schematic of the optical system for evaluating the structural color effect. (For interpretation of the references to color in this figure legend, the reader is referred to the Web version of this article.)

system, which can command the employed axes to move as dictated by the developed optimized tool paths. The main experimental parameters are summarized in Table 2.

In order to validate the feasibility of proposed rendering principle and the global optimization algorithm, the structural color effect was studied with the aid of an optical system as illustrated in Fig. 7(b). A digital single-lens reflex (DSLR) camera mounted with a 100-mm macro lens was placed perpendicularly to the sample surface to match the assumption of observing angle in the principle section. The camera white balance was calibrated using a white paper under the test illumination condition. Then, the exposure and aperture for each shot were set the same in order to accurately evaluate the brightness of structural color. Besides, a commercially available LED parallel white light source was employed to illuminate the machined samples from the direction perpendicular to the grating structures. The parallel white light source was mounted on a flexible frame to achieve adjustable incident angles (θ_i). The whole shooting process was carried out in a darkroom to prevent possible noises caused by different external lighting conditions.

5.2. Ultrasonic modulation cutting of high-resolution images

Experiments were carried out to verify the effectiveness and feasibility of developed optimization methods by commanded the cutting axis to move as dictated by the optimized tool paths. The in-situ position of motion axis was recorded using a non-contact linear encoder mounted on the cutting axis under a sampling rate of 8 kHz. Since the running time for each *PVT* movement is set to be larger 10 ms, the real-time feedback velocity of the cutting axis can be calculated by assuming constant velocity between two nearby sampling periods and compared with the optimized tool velocity profiles.

The reproduced high-resolution images textured with the tool path optimized by the equal segment length optimization method are shown in Fig. 8(a) and Fig. 9(a) with similar processing time around 6 min, while the comparisons between the real-time velocity profiles and commanded tool paths are illustrated in Figs. 8(b) and Fig. 9(b). The vivid reproduced color images show great similarities to the simulated results, which evidences the effectiveness of proposed simulation model. The minor image differences were attributed to the varying color saturation and brightness at each pixel on the textured images, which was not included in the simulation model. The saturation and brightness variation were mainly related to the varying diffraction efficiency of grating structures with different spacing distances and varying response sensitivity at different wavelengths of employed CMOS imaging sensors. Moreover, the feasibility of optimized tool

paths has been proved by the tracking performance of real-time tool paths to the optimized velocity profiles consisting of a series of spline curves. For the equal segment length optimization method with 10 pixels in each segment, the unexpected regular fringe patterns on the simulated result were also identified on some orange color regions of the reproduced image. Due to the significant integer rounding error of running time in each limited length segment, the uniform deviation of optimized tool velocity from objective tool path will be raised on some consecutive segments containing steady objective velocity profile and lead to the regular fringe patterns on the reproduced image. For the equal segment length of 40 pixels, the impact of integer rounding error of running time has been weakened to some extent while the fitting accuracy is greatly reduced due to the increased pixel number for each fitting segment. Therefore, the reproduced image is though quite smooth and vivid but distinctly distorted and blurred compared to the original one.

Textured with the globally optimized tool path, the rendered high-resolution image almost perfectly restores the original image with clear image main contours as well as vivid and smooth color information as shown in Fig. 10(a) with a processing duration around 6 min. The image main contour points were serving as the control points in the global optimization method. Due to the acceleration discontinuity at the control points, distinct image contours will be displayed on the textured color image, which accounts for the fact that the experimental result outperforms the simulated one shown in Fig. 6(c). In addition, the

Table 2
Machining parameters for high-resolution images reproduction.

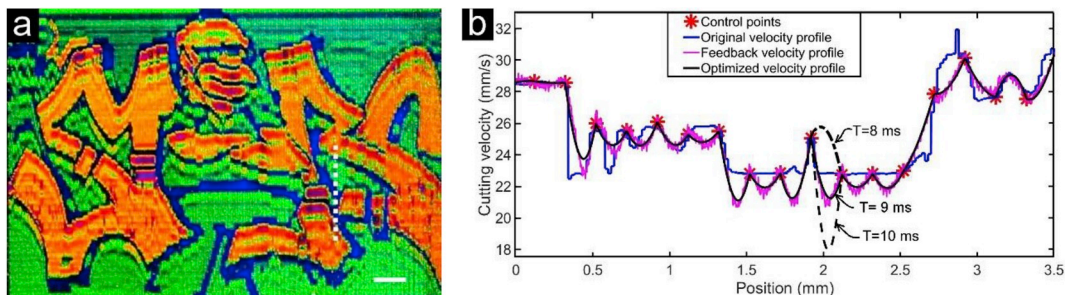| Cutting tool	Material:	Single crystalline diamond
	Rake angle:	0°
	Clearance angle:	12°
	Nose radius	200 μm
Vibration parameters	Amplitudes (peak to peak)	6 μm in depth-of cut direction
		2 μm in cutting direction
	Frequency	30.85 kHz
Cutting parameters	Cross feed (Y)	40 μm
	Depth-of-cut (Z)	2 μm
Workpiece	Material	Brass
	Textured area	9.7 × 14.0 mm

22

Fig. 8. (a) Captured high-resolution image machined with the optimized tool path for equal segment length of 10 pixels; and (b) comparison among the feedback, commanded, and objective velocity profiles of the dotted line in (a). Scale bar is 1 mm.

developed global optimization method will give the optimal division solution for each cutting line considering the limitation of integer running time for individual spline function. The integer rounding error of running time has been greatly reduced without the loss of overall fitting accuracy by recursively searching the optimal pixel number for each segment as shown in Fig. 10(b). Hence, the unexpected fringe patterns have been eliminated on the same color region and the overall rendering performance is further increased compared with the equal segment length method of 10 pixel. Moreover, considering the feasibility of optimized tool velocity profile, the average fitting error of actual tool path to the objective one reaches 0.9 mm/s for each pixel corresponding to the grating spacing deviation less than 30 nm.

5.3. Image similarity comparison and optical variable effect

To quantitively evaluate the reproduced image quality, it is necessary to employ an image comparison method to determine the similarity of reproduced image to the original one. Here, a universal image quality evaluation algorithm is adopted, where the image distortion is modeled as a combination of loss of correlation, luminance distortion, and contrast distortion [29]. The derived image quality index is more

an indication of color difference at each pixel of reproduced image and a direct reflection of approximation accuracy for different toolpath optimization methods, which would be less consistent with human eye perception that mainly focuses on the image main characteristic representation. Two identical images will give a quality index of 1. Taking the original image as a perfect image, the quality indices for the simulated and machined images obtained from different optimized tool paths have been listed in Table 3. The results reveal that the quality indices of textured images are not the same as simulated ones but show a similar trend in terms of different optimization methods. The main reasons are attributed to that the brightness and saturation of the textured images are related to the external illumination condition, CMOS image sensor sensitivity, and diffraction efficiency of constituent pixels, while they are assumed to be identical in the simulation model. Nevertheless, the quality index of textured image machined with the global optimal tool path is larger than those with equal segment divisions, which supports the validity of proposed global tool path optimization algorithm in a quantitative manner.

Based on the underlying mechanism of diffractive structural color, the apparent color varies with the observing angle and/or the incident angle of illumination light, which enables the optical variable effect of
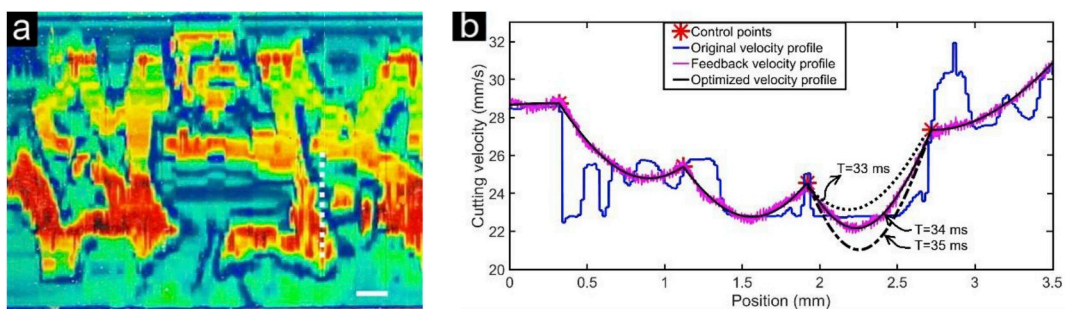

Fig. 9. (a) Captured high-resolution image machined with the optimized tool path for equal segment length of 40 pixels; and (b) comparison among the feedback, commanded, and objective velocity profiles of the dotted line in (a). Scale bar is 1 mm.
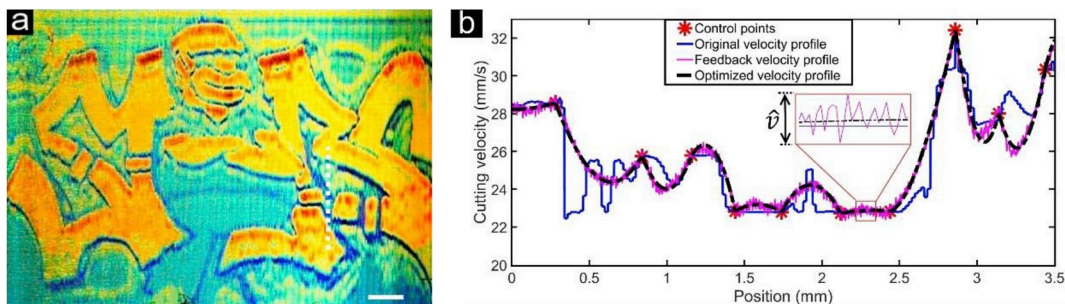

Fig. 10. (a) Captured high-resolution image machined with the global optimized tool path; and (b) comparison among the feedback, commanded, and objective velocity profiles of the dotted line in (a). Scale bar is 1 mm.

Table 3
Quality index of the simulated and machined images.

	Equal segment length of 10 pixels	Equal segment length of 40 pixels	Global optimization method
Simulated image	0.93	0.93	0.96
Textured image	0.78	0.85	0.87
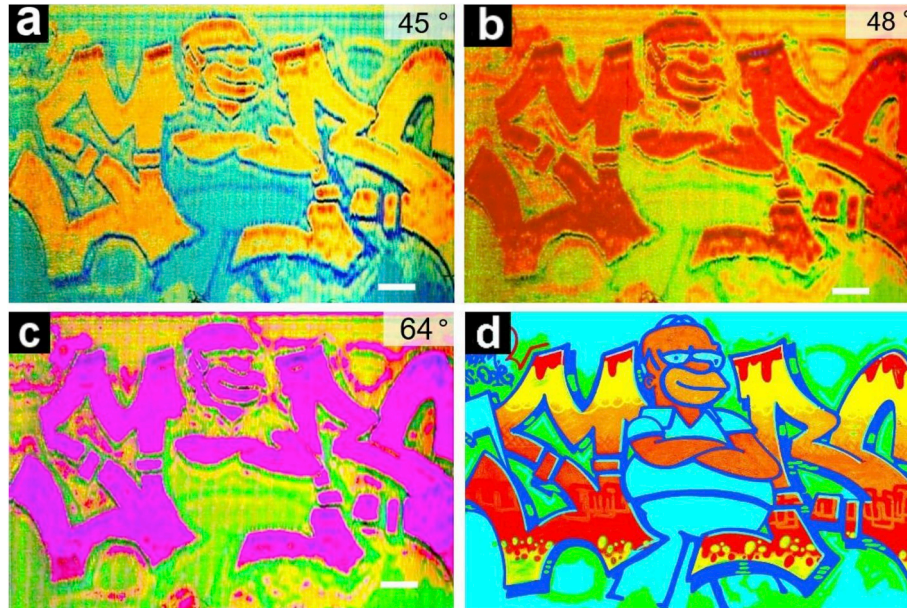
Fig. 11. Optical variable effect of textured sample under various incident angles of the illumination light: (a) 45°; (b) 48°; (c) 64° and (d) original image. Scale bar is 1 mm.

textured images. The optical variable effect of machined samples with the proposed global optimal tool path is demonstrated in Fig. 11, which may find potential applications in anti-counterfeiting field by transferring structural color onto polymer substrates using injection molding or roll-to-roll processes [30]. The captured color image under a specific incident angle of illumination light can be predicted by applying the similar analysis presented in section 2.2. The overall structural color will have redshifts when the incident angle gradually increases from the design value of 45°. In addition, since the maximal grating spacing (1 μm) is larger than twice of the wavelength of violet light (0.41 μm ~ 0.45 μm), higher order diffractive light will be introduced for a large incident angle of illumination condition as shown in Fig. 11(c).

6. Conclusions

In this paper, a rendering strategy for grating-induced high-resolution image reproduction has been proposed based on tool path planning. The following conclusions can be drawn based on the above results and analyses.

1. The feasibility of rendering high-resolution images with pre-defined color at each pixel using diffractive structural color has been theoretically revealed. Accurate reproduction of the high-resolution image can be established by planning the tool path to achieve a piecewise step function of velocity profile, where a constant velocity is specified inside each pixel of the color image.
2. A recursive optimization method has been proposed to provide a global optimal tool path to approximate the objective tool velocity profile utilizing a series of cubic polynomial tool paths in terms of minimum overall velocity error. The feasible region of pixel number

in each cubic spline movement is determined under the consideration of minimum sampling period and acceleration bound of the employed motion axis to guarantee the feasibility of optimized tool path.
3. The overall fitting accuracy of global optimized tool path outperforms the intuitive equal segment length optimization methods. Meanwhile, the simulated image based on the global optimized tool path shows distinct image main contours together with smooth and vivid gradient color information of the original image that could not be achieved simultaneously by the intuitive equal segment length optimization methods, which supports the global optimality of the proposed method.
4. The experimental studies validated the feasibility of optimized tool path and the effectiveness of the simulation model. The recursive optimization method is capable of finding the optimal division to reduce the integer rounding error effect of running time without the loss of overall fitting accuracy. The main characteristics and details of simulated images were captured in the textured results and supported by the comparison between the real-time tool velocity-location profile and the objective curve.
5. The quality of reproduced color images is quantitively evaluated through a universal image quality evaluation algorithm. The results indicate the effectiveness of proposed global optimization method for tool path planning. The optical variable effect of machined high-resolution image is demonstrated.

Northwestern University, Evanston, IL, USA.

Appendix B. Supplementary data

Supplementary data related to this article can be found at https://doi.org/10.1016/j.ijmachtools.2018.11.002.

Appendix A. Calibration process for the mapping function linking the color hue and diffracted wavelength

By commanding a constant cutting velocity during the coloration process, grating structures with unique spacing distance can be obtained. As shown in Fig. A1(a), the color pallets were textured by selecting suitable nominal cutting velocities to generate grating structures with unique spacing distances ranging from 0.56 μm to 1.00 μm with an increment of 0.04 μm. Various color pallets have been captured under different incident angles of parallel illumination light. According to the basic grating equation, different diffracted colors will be captured by either varying the grating spacing distance or incident angle of parallel illumination white light. The color brightness and saturation variation for each color block are mainly attributed to the varying diffraction efficiency of grating structures with different spacing distances and varying response sensitivity at different wavelengths of employed CMOS imaging sensors. Therefore, black color blocks are displayed when the wavelengths of diffracted light are beyond the spectral response range of imaging sensors. Nevertheless, the linear mapping function can be derived by mapping the hue of captured color to the wavelength with minimum least squares error respect to the theoretical wavelength given by Eq. (2) under different illuminating and observing conditions. The approximation performance of calibrated linear mapping function has been shown in Fig. A1(b), which matches well with basic grating equation. In addition, the full color pallet with light wavelength covered the whole visible spectrum can be achieved when the incident angle of illumination light is kept at 45°.
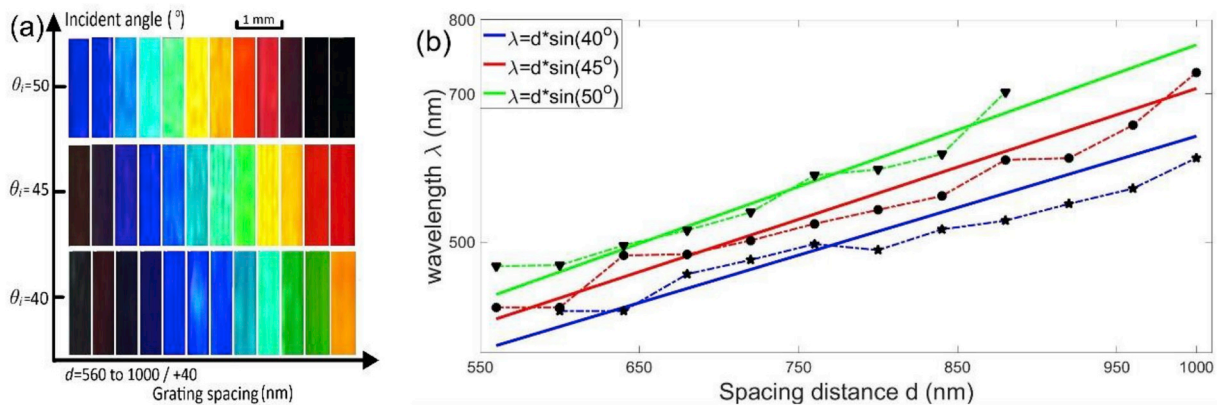

Fig. A1. (a) Color pallets captured under different incident angles of illumination light; and (b) approximation performance of calibrated linear mapping function from the color hue to the diffracted light wavelength under different illumination conditions.

References

[1] G. Tayeb, B. Gralak, S. Enoch, Structural colors in nature and butterfly-wing modeling, Optic Photon. News 14 (2003) 38–43.
[2] J. Zi, X. Yu, Y. Li, X. Hu, C. Xu, X. Wang, X. Liu, R. Fu, Coloration strategies in peacock feathers, Proc. Natl. Acad. Sci. Unit. States Am. 100 (2003) 12576–12578.
[3] M. Srinivasarao, Nano-optics in the biological world: beetles, butterflies, birds, and moths, Chem. Rev. 99 (1999) 1935–1962.
[4] J. Xue, Z.K. Zhou, Z. Wei, R. Su, J. Lai, J. Li, C. Li, T. Zhang, X.H. Wang, Scalable, full-colour and controllable chromotropic plasmonic printing, Nat. Commun. 6 (2015) 8906.
[5] K. Kumar, H. Duan, R.S. Hegde, S.C. Koh, J.N. Wei, J.K. Yang, Printing colour at the optical diffraction limit, Nat. Nanotechnol. 7 (2012) 557.
[6] A.Y. Vorobyev, C. Guo, Colorizing metals with femtosecond laser pulses, Appl. Phys. Lett. 92 (2008) 041914.
[7] B. Dusser, Z. Sagan, H. Soder, N. Faure, J.P. Colombier, M. Jourlin, E. Audouard, Controlled nanostructrures formation by ultra fast laser pulses for color marking, Optic Express 18 (2010) 2913–2924.
[8] S.J. Tan, L. Zhang, D. Zhu, X.M. Goh, Y.M. Wang, K. Kumar, C.W. Qiu, J.K. Yang, Plasmonic color palettes for photorealistic printing with aluminum nanostructures, Nano Lett. 14 (2014) 4023–4029.
[9] Y. Yang, Y. Pan, P. Guo, Structural coloration of metallic surfaces with micro/nano-structures induced by elliptical vibration texturing, Appl. Surf. Sci. 402 (2017) 400–409.
[10] P. Guo, K.F. Ehmann, An analysis of the surface generation mechanics of the elliptical vibration texturing process, Int. J. Mach. Tool Manufact. 64 (2013) 85–95.
[11] P. Guo, Y. Lu, K.F. Ehmann, J. Cao, Generation of hierarchical micro-structures for anisotropic wetting by elliptical vibration cutting, CIRP Ann. - Manuf. Technol. 63 (2014) 553–556.
[12] P. Guo, K.F. Ehmann, Development of a tertiary motion generator for elliptical vibration texturing, Precis. Eng. 37 (2013) 364–371.
[13] N. Suzuki, H. Yokoi, E. Shamoto, Micro/nano sculpturing of hardened steel by

[14] controlling vibration amplitude in elliptical vibration cutting, Precis. Eng. 35 (2011) 44–50.
[14] R. Huang, X. Zhang, W.K. Neo, A.S. Kumar, K. Liu, Ultra-precision Machining of Grayscale Pixelated Micro Images on Metal Surface, Precision Engineering, 2017.
[15] C.H. Chu, J.T. Chen, Tool path planning for five-axis flank milling with developable surface approximation, Int. J. Adv. Manuf. Technol. 29 (2006) 707.
[16] W. Sheng, H. Chen, N. Xi, Y. Chen, Tool path planning for compound surfaces in spray forming processes, IEEE Trans. Autom. Sci. Eng. 2 (2005) 240–249.
[17] H.T. Hsieh, C.H. Chu, Improving optimization of tool path planning in 5-axis flank milling using advanced PSO algorithms, Robot. Comput. Integrated Manuf. 29 (2013) 3–11.
[18] W. Zhong, X. Luo, W. Chang, F. Ding, Y. Cai, A real-time interpolator for parametric curves, Int. J. Mach. Tool Manufact. 125 (2018) 133–145.
[19] M. Heng, K. Erkorkmaz, Design of a NURBS interpolator with minimal feed fluctuation and continuous feed modulation capability, Int. J. Mach. Tool Manufact. 50 (2010) 281–293.
[20] K. Erkorkmaz, M. Heng, A heuristic feedrate optimization strategy for NURBS toolpaths, CIRP Ann. - Manuf. Technol. 57 (2008) 407–410.
[21] K. Zhang, C.M. Yuan, X.S. Gao, Efficient algorithm for time-optimal feedrate planning and smoothing with confined chord error and acceleration, Int. J. Adv. Manuf. Technol. 66 (2013) 1685–1697.
[22] A. Olabi, R. Béarée, O. Gibaru, M. Damak, Feedrate planning for machining with industrial six-axis robots, Contr. Eng. Pract. 18 (2010) 471–482.
[23] P. Guo, Y. Lu, P. Pei, K.F. Ehmann, Fast generation of micro-channels on cylindrical surfaces by elliptical vibration texturing, J. Manuf. Sci. Eng. 136 (2014) 041008.
[24] Y. Yang, P. Guo, Fast generation of planar microstructured surfaces by elliptical vibration texturing, J. Micro Nano-Manufacturing 5 (2017) 011004.
[25] Y. Yang, S. Gao, K. Chen, Y. Pan, P. Guo, Vibration analysis and development of an ultrasonic elliptical vibration tool based on a portal frame structure, Precis. Eng. 50 (2017) 421–432.
[26] Z. Ou, M. Huang, F. Zhao, Colorizing pure copper surface by ultrafast laser-induced near-subwavelength ripples, Optic Express 22 (2014) 17254–17265.

[27] K. Yoon, S. Choi, J. Paek, D. Im, J. Roh, J. Kwon, H. Kim, Iridescent specular structural colors of two-dimensional periodic diffraction gratings, J. Opt. Soc. Korea 18 (2014) 616–622.

[28] K.N. Plataniotis, A.N. Venetsanopoulos, Color Image Processing and Applications, Springer Science and Business Media, 2013.

[29] Z. Wang, A.C. Bovik, A universal image quality index, IEEE Signal Process. Lett. 9

(2002) 81–84.

[30] C. Koidis, S. Logothetidis, S. Kassavetis, C. Kapnopoulos, P.G. Karagiannidis, D. Georgiou, A. Laskarakis, Effect of process parameters on the morphology and nanostructure of roll-to-roll printed P3HT: PCBM thin films for organic photovoltaics, Sol. Energy Mater. Sol. Cell. 112 (2013) 36–46.